Electronic Supplementary Material (ESI) for Journal of Materials Chemistry A.

Photo-enhanced electrocatalysis of sea-urchin shaped $Ni_3(VO_4)_2$ for hydrogen evolution reaction

Bin Chang, Gang Zhao, Yongliang Shao, Lei Zhang, Baibiao Huang, Yongzhong Wu*, Xiaopeng Hao*

State Key Lab of Crystal Materials, Shandong University, Jinan, 250100, China
Email: wuyz@sdu.edu.cn; xphao@sdu.edu.cn

S1 Morphological evolution of the as-prepared $Ni_3(VO_4)_2$ with reaction times

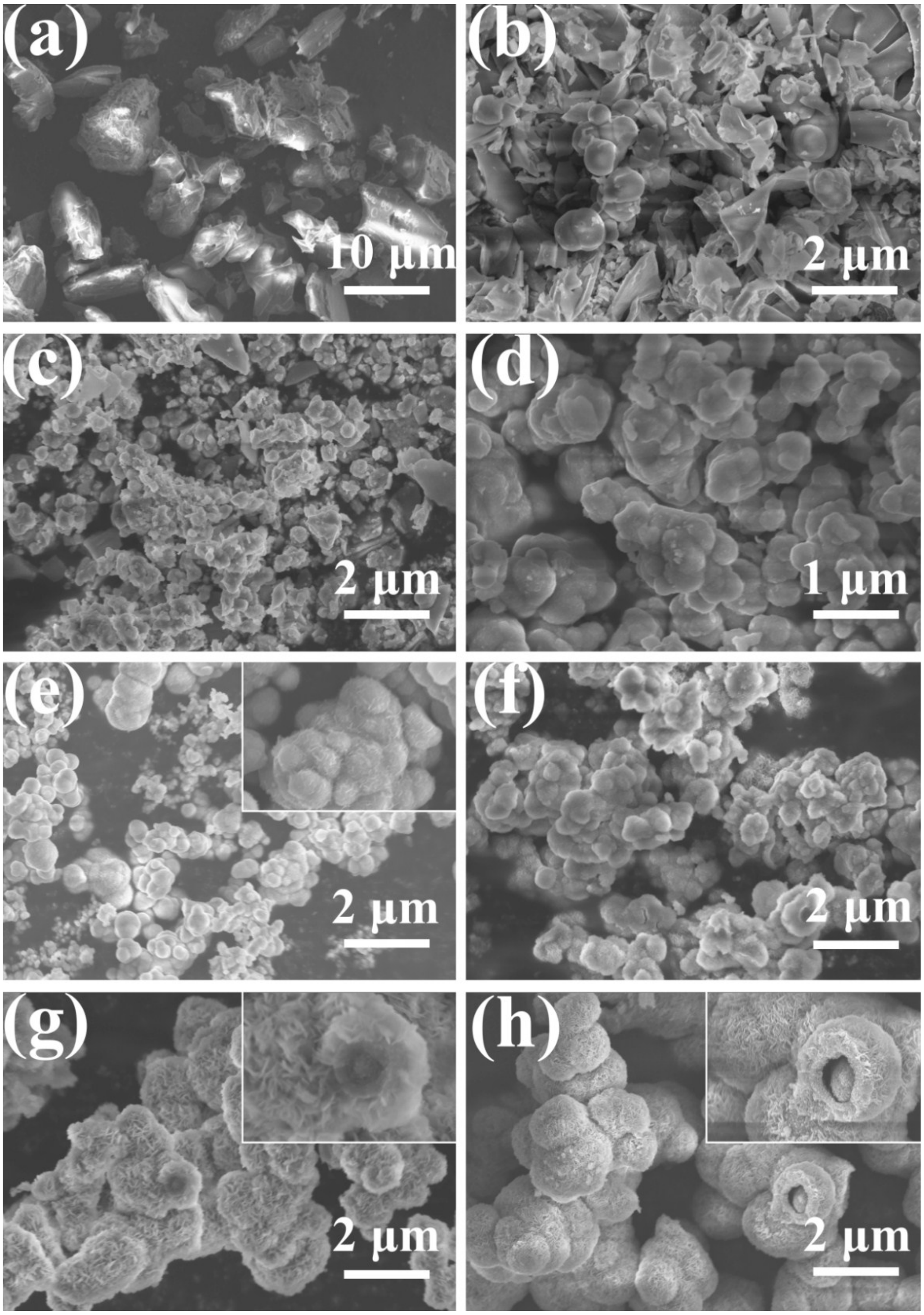

Figure S1 Morphological evolution of the sea-urchin shaped $Ni_3(VO_4)_2$ prepared at 200 ^oC at different reaction times: 0 h (a), 0.5 h (b), 1 h (c), 2 h (d), 4 h (e), 8 h (f), 12h (g), and 18 h (h).

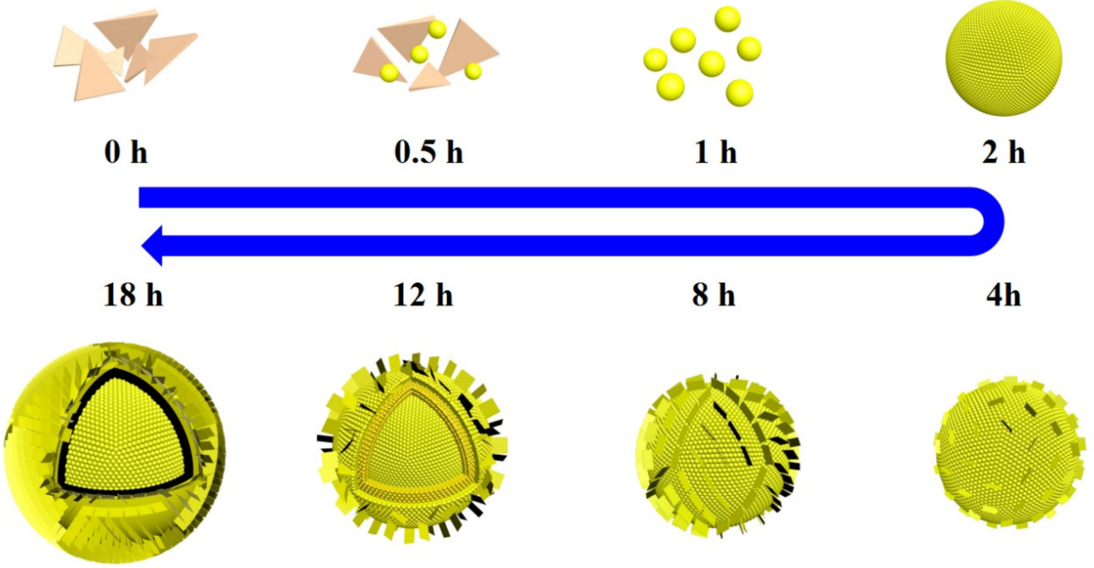

Figure S2 Schematic illustration of the formation process of the sea-urchin shaped $Ni_3(VO_4)_2$.

Here, sea-urchin shaped $Ni_3(VO_4)_2$ was successfully synthesized through a simple approach employing temperature (200 °C) reaction of $Ni(NO_3)_2 \cdot 6H_2O$, NH_4VO_3, and DTAB in homogeneous solution of ethanediol and H_2O. The formation process of sea-urchin structure is schematically illustrated in Fig. S2. In the initial stages, a large number of intermediate nuclei were formed the solvothermal treatment in a short time (Fig. S1a-c) and aggregated to large spheres (Fig. S1d) through the reaction between $Ni(NO_3)_2$, NH_4VO_3 and DTAB in a homogeneous solution. Then, slow crystal growth followed: nanoflakes were grown on the surfaces due to their propensity for two-dimensional growth (Fig. S1e, f). The nanoflakes located on the outside surface would serve as starting points for the subsequent crystallization process (Fig. S1g), and then an interior cavity and an inner core were gradually formed via a core evacuation process due to higher surface energies (Fig. S1h).[1-3]

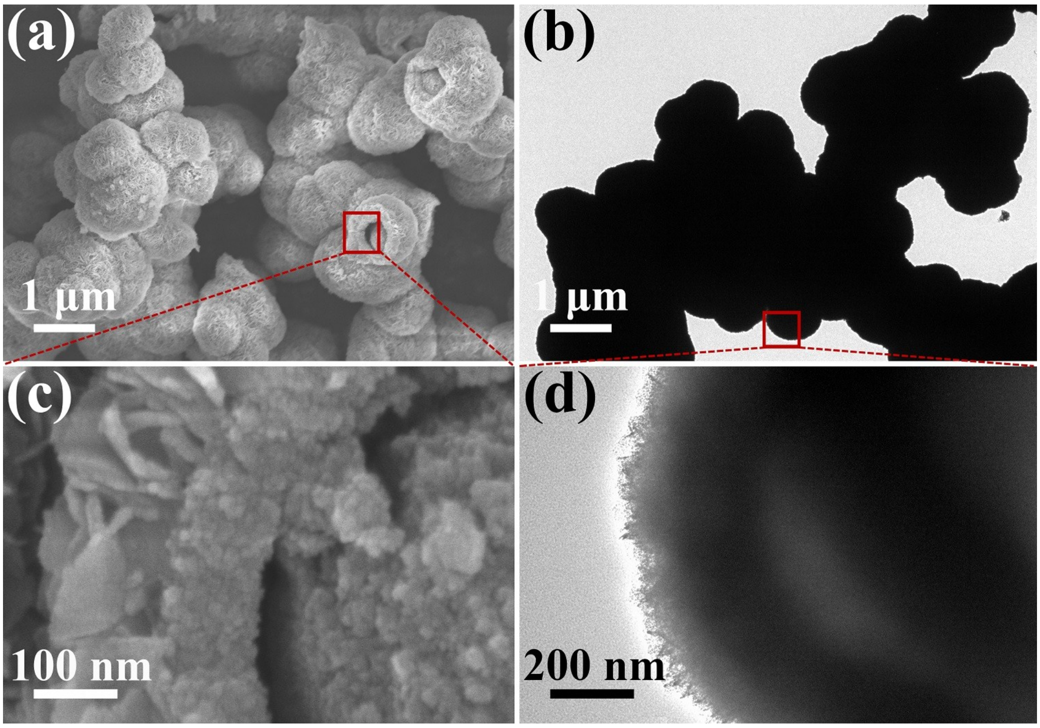

Figure S3 Morphology of the sea-urchin shaped $Ni_3(VO_4)_2$. a, c) SEM images of the as-synthesized specimen. b, d) TEM images of the as-synthesized specimen.

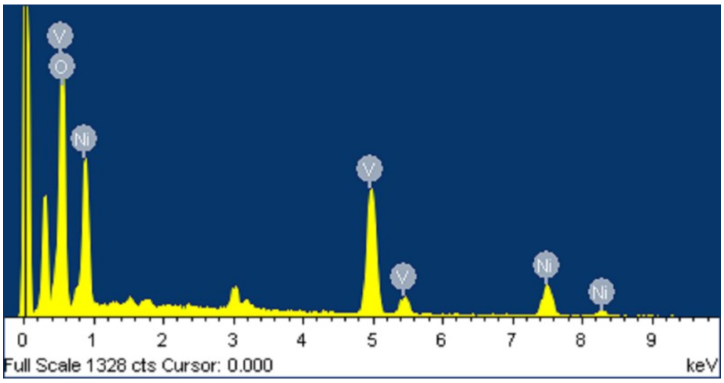

Figure S4 EDS spectrum of the sea-urchin shaped $Ni_3(VO_4)_2$.

Table S1. EDS elements analyze of the sea-urchin shaped $Ni_3(VO_4)_2$.

Element	Weight%	Atomic%
O K	34.53	64.68
V K	24.17	14.22
Ni K	41.30	21.09
Totals	100.00	

There are nickel (Ni), vanadium (V) and oxygen (O) elements in the EDS spectrum of $Ni_3(VO_4)_2$ (Figure S4). The atomic ratio of nickel and vanadium is nearly 3:2. The atomic content of oxygen is a little larger than theoretical value. We conclude that the small amount of redundant oxygen may be introduced from the residual surfactant (DTAB) in the preparation process. The peak beside O peak belongs to C, which is due to the use of carbon tape as the substrate in testing process.

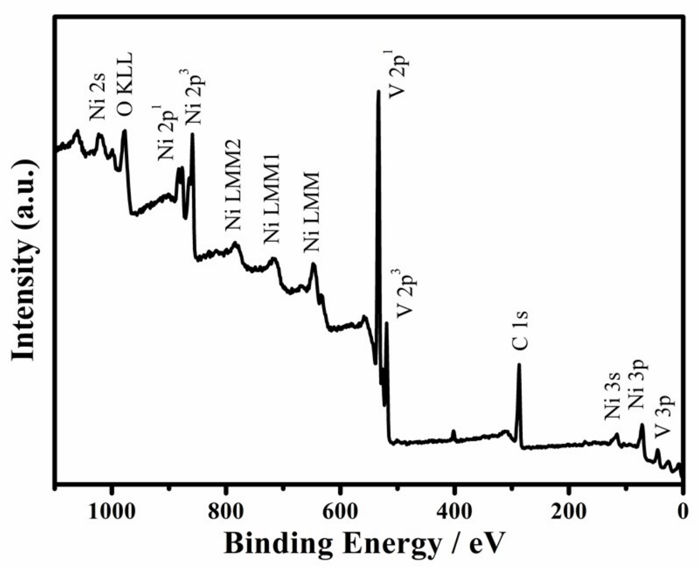

Figure S5 The XPS survey spectrum of $Ni_3(VO_4)_2$ catalysts.

S2 Comparison of the morphology and electrocatalytic HER activity of the sea-urchin shaped $Ni_3(VO_4)_2$ and Ni_xV_{1-x} materials

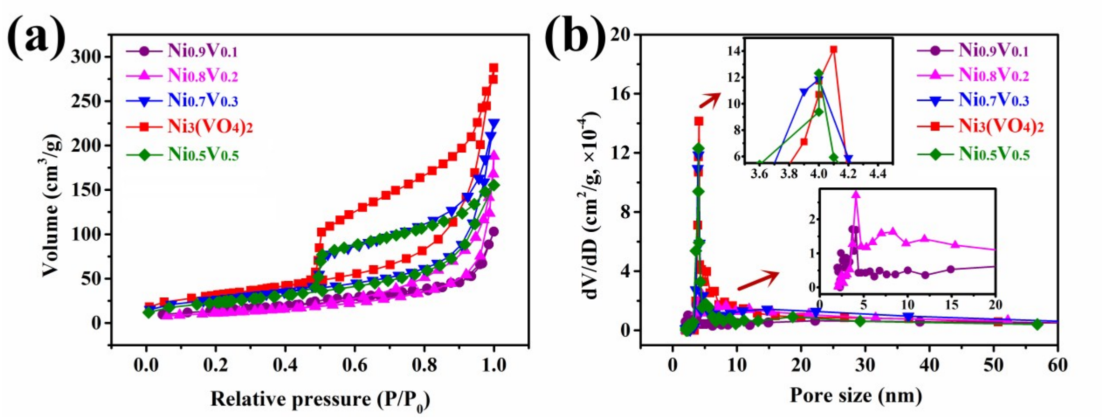

Figure S6 (a) BET surface area of the sea-urchin shaped $Ni_3(VO_4)_2$ and Ni_xV_{1-x} materials ($Ni_{0.9}V_{0.1}$, $Ni_{0.8}V_{0.2}$, $Ni_{0.7}V_{0.3}$ and $Ni_{0.5}V_{0.5}$). (b)The corresponding pore size distribution of the as-synthesized specimen above.

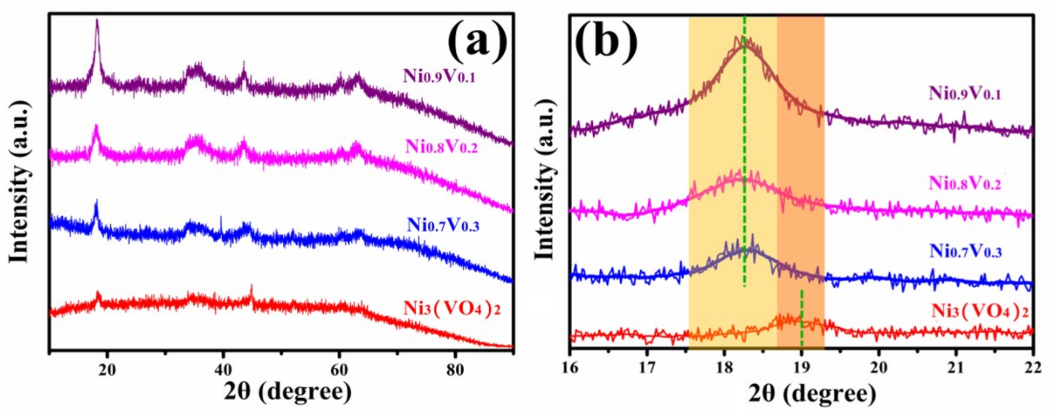

Figure S7 (a) XRD patterns of the sea-urchin shaped $Ni_3(VO_4)_2$ and Ni_xV_{1-x} materials ($Ni_{0.9}V_{0.1}$, $Ni_{0.8}V_{0.2}$ and $Ni_{0.7}V_{0.3}$). (b) The corresponding enlarged drawing of a.

The excessive nickel transfer to $Ni(OH)_2$ in the Ni_xV_{1-x} materials ($Ni_{0.9}V_{0.1}$, $Ni_{0.8}V_{0.2}$ and $Ni_{0.7}V_{0.3}$). As is shown in Figure S7 a-b, the characteristic peaks of $Ni(OH)_2$ at 18.3° which covered one of the diffraction peaks of $Ni_3(VO_4)_2$ at 19.0° are attenuated with the decrease of excessive nickel.[4] Once again these results confirm that optimizing the initial raw material proportion of nickel and vanadium (3:2) gives rise to the formation of single $Ni_3(VO_4)_2$ without any impurities.

Table S2. ICP analyze of $Ni_3(VO_4)_2$ and Ni_xV_{1-x} materials

Samples	Ni(58.70) ppm	V(50.94) ppm	The ratio of elements [a] (%)	The theoretical ratio of elements (%) [a]
$Ni_{0.9}V_{0.1}$	75.72	7.44	8.834	9.000
$Ni_{0.8}V_{0.2}$	53.14	11.97	3.852	4.000
$Ni_{0.7}V_{0.3}$	58.51	20.70	2.453	2.333
$Ni_3(VO_4)_2$	62.32	36.84	1.468	1.500
$Ni_{0.5}V_{0.5}$	47.09	40.99	0.997	1.000
$Ni_{0.4}V_{0.6}$	52.66	66.71	0.685	0.667

[a] The ratio of elements = mole number of nickel / mole number of vanadium.

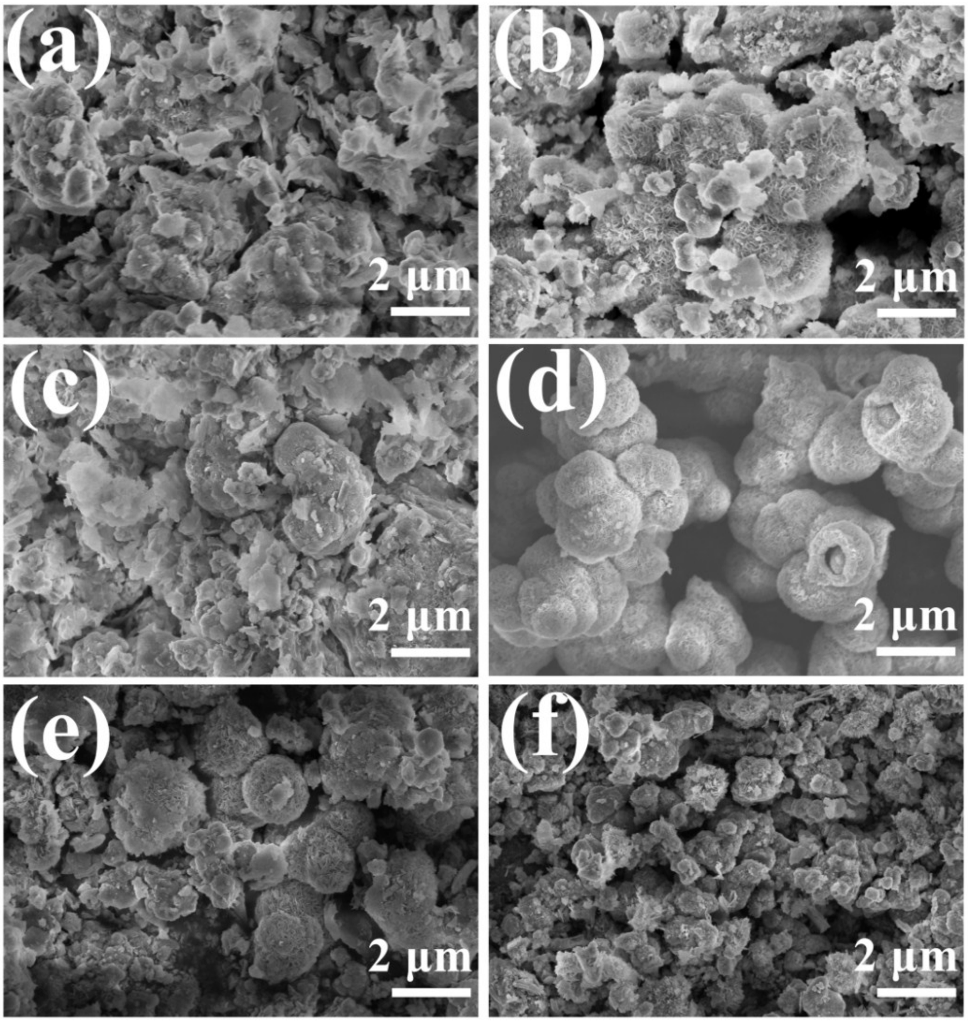

Figure S8 SEM images of $Ni_{0.9}V_{0.1}$ (a), $Ni_{0.8}V_{0.2}$ (b), $Ni_{0.7}V_{0.3}$ (c), $Ni_3(VO_4)_2$ (d), $Ni_{0.5}V_{0.5}$ (e) and $Ni_{0.4}V_{0.6}$ (f).

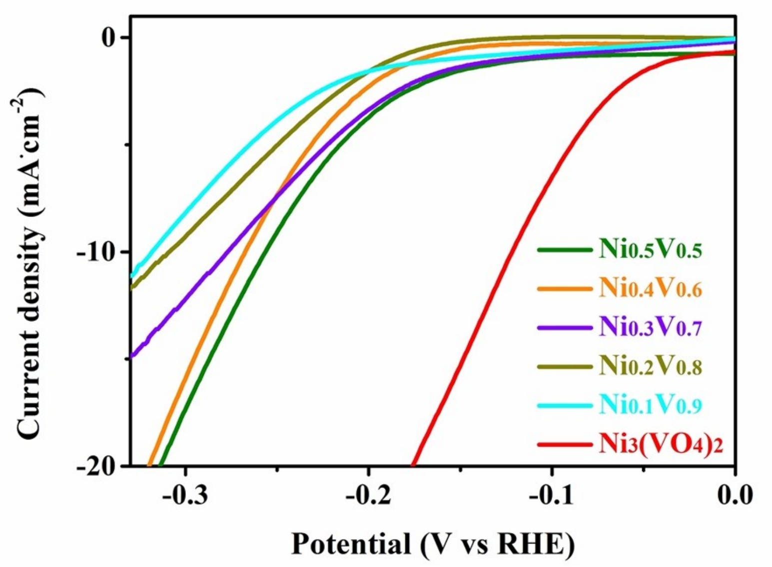

Figure S9 Polarization curves of the sea-urchin shaped $Ni_3(VO_4)_2$, the Ni_xV_{1-x} materials of lower Ni ratios (x means ratios of nickel) with a scan rate of 0.5 mV·s^{-1} in 0.5 M H_2SO_4.

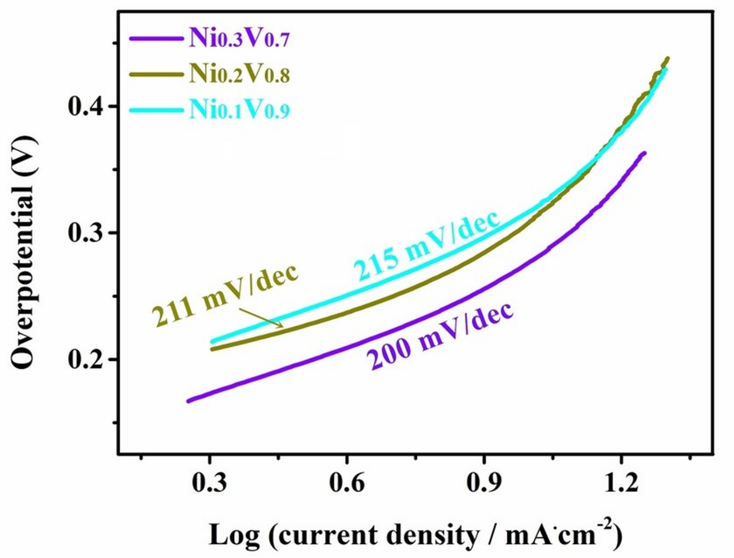

Figure S10 Tafel plots of $Ni_{0.3}V_{0.7}$, $Ni_{0.2}V_{0.8}$ and $Ni_{0.1}V_{0.9}$ derived from Figure S9.

The polarization curves show the overpotentials needed for $Ni_{0.3}V_{0.7}$, $Ni_{0.2}V_{0.8}$ and $Ni_{0.1}V_{0.9}$ to achieve a catalytic current density of 10 mA·cm^{-2} are 277, 309 and 318 mV versus RHE, respectively (Fig. S9). As shown in Fig. S10, the Tafel slope of $Ni_{0.3}V_{0.7}$, $Ni_{0.2}V_{0.8}$ and $Ni_{0.1}V_{0.9}$ are ~200 mV/decade, ~211 mV/decade and 215 mV/decade, respectively.

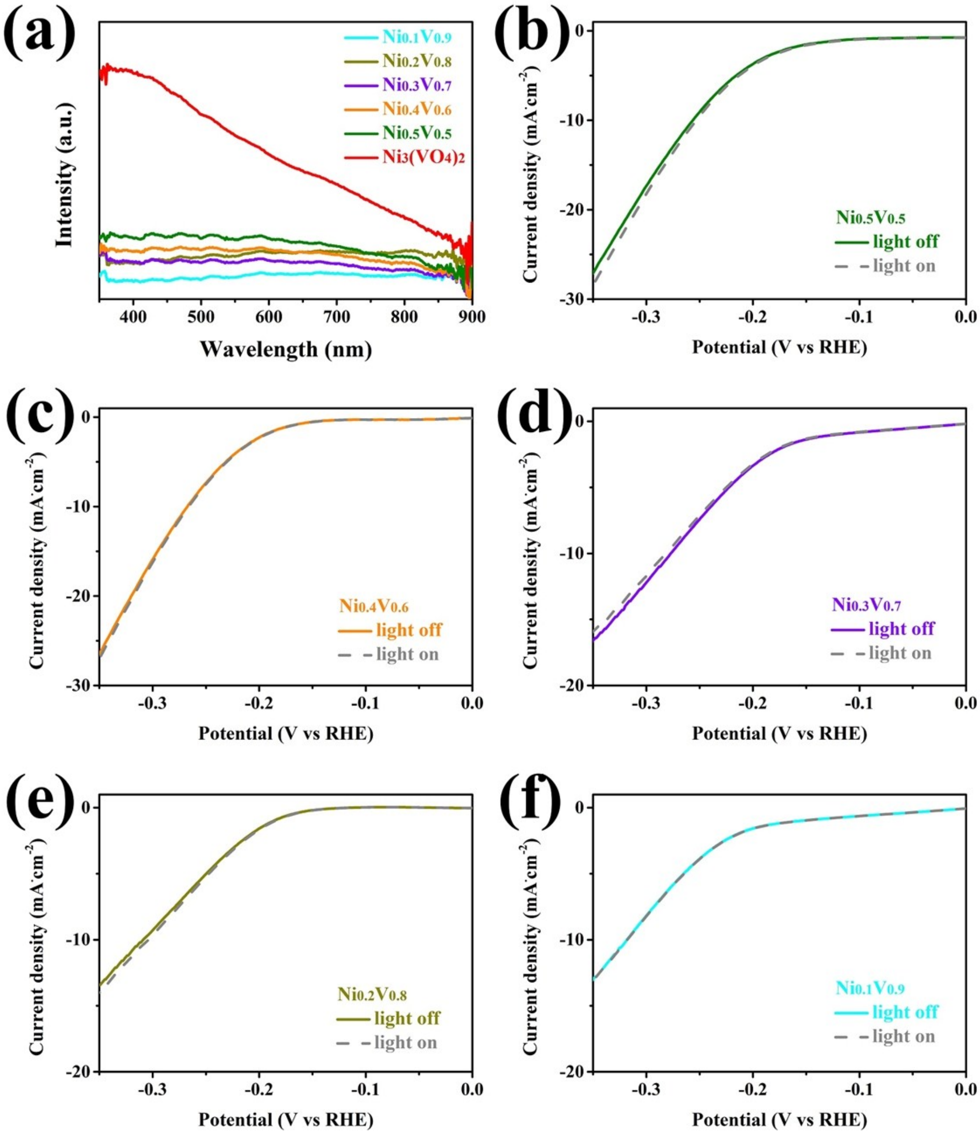

Figure S11 a) UV-vis DRS on $Ni_3(VO_4)_2$ and samples of lower Ni ratios. b-f)The comparison of the polarization curves of $Ni_{0.5}V_{0.5}$, $Ni_{0.4}V_{0.6}$, $Ni_{0.3}V_{0.7}$, $Ni_{0.2}V_{0.8}$ and $Ni_{0.1}V_{0.9}$ before and after visible light irradiation.

The results of the UV-vis diffuse reflectance spectroscopy (UV-vis DRS) on $Ni_3(VO_4)_2$ and samples of lower Ni ratios are shown in Fig. S11a. It can be observed in Fig. S13a that the samples of the samples of lower Ni ratios ($Ni_{0.5}V_{0.5}$, $Ni_{0.4}V_{0.6}$, $Ni_{0.3}V_{0.7}$, $Ni_{0.2}V_{0.8}$ and $Ni_{0.1}V_{0.9}$) all act out very weak or even no visible light absorption. Besides, in the catalytic system above, there is no enhancement of the electrocatalytic HER activity under visible light irradiation (Fig. S11 b-f).

S3 Experiments of the stability of the sea-urchin shaped $Ni_3(VO_4)_2$ in HER electrocatalysis

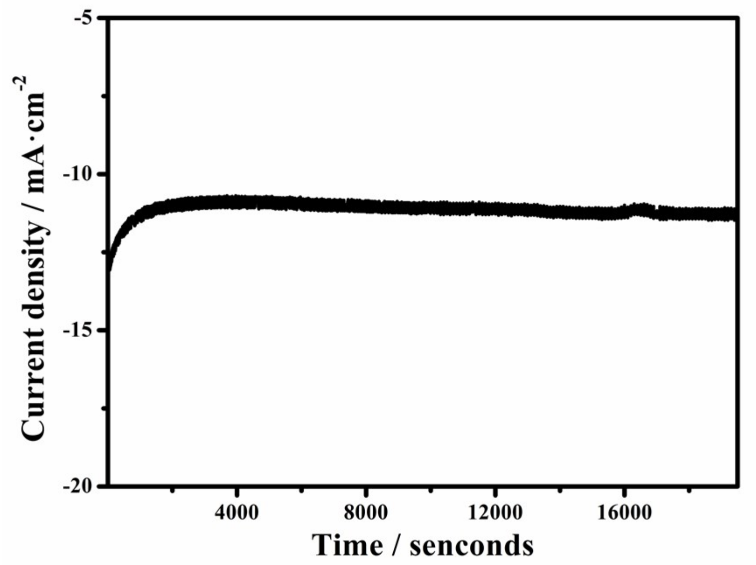

Figure S12 Time-dependent current density curve under static overpotential of 120 mV. The measurement was conducted in 0.5 M H_2SO_4.

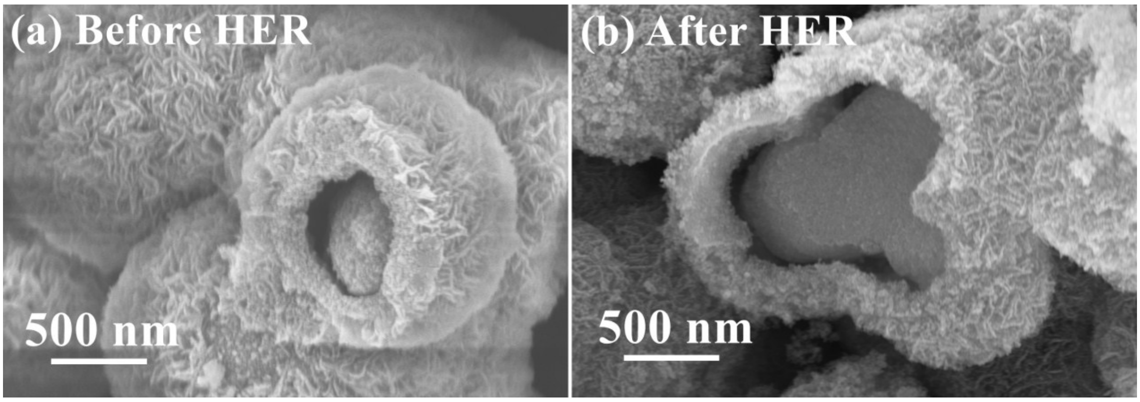

Figure S13 SEM images of the sea-urchin shaped $Ni_3(VO_4)_2$ before (a) and after (b) the stability test.

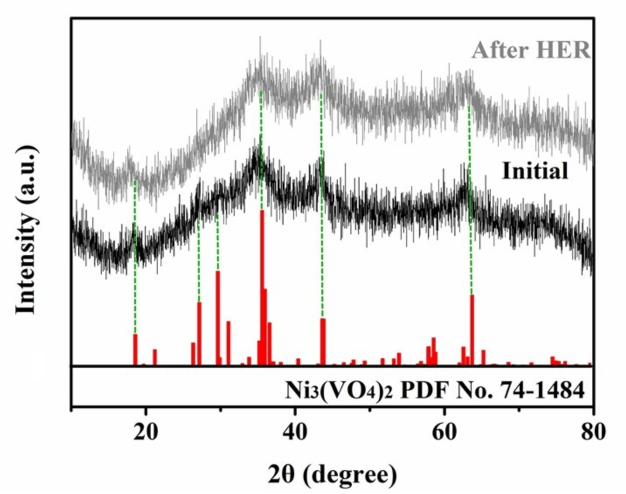

Figure S14 XRD patterns of the sea-urchin shaped $Ni_3(VO_4)_2$ before and after the PEC stability test.

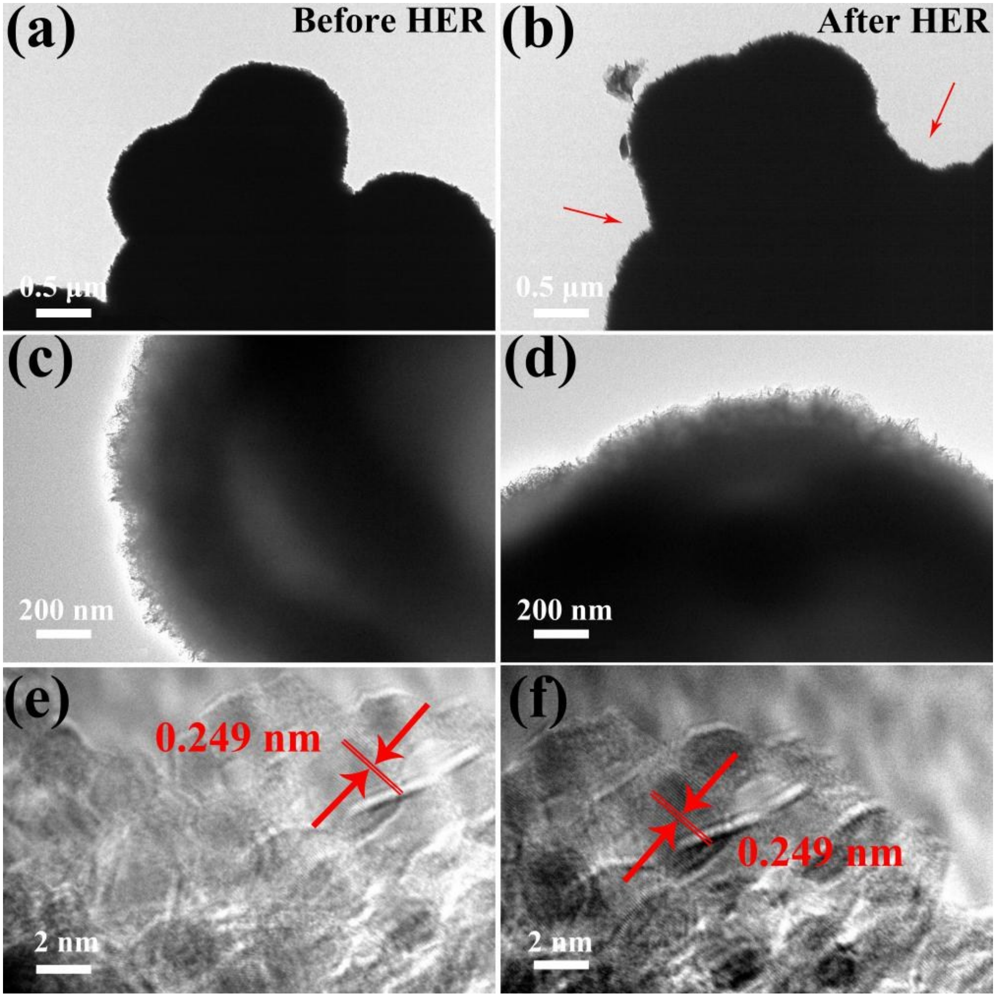

Figure S15 TEM and HR-TEM images of the sea-urchin shaped $Ni_3(VO_4)_2$ before (a, c, e) and after (b, d, f) the PEC stability test.

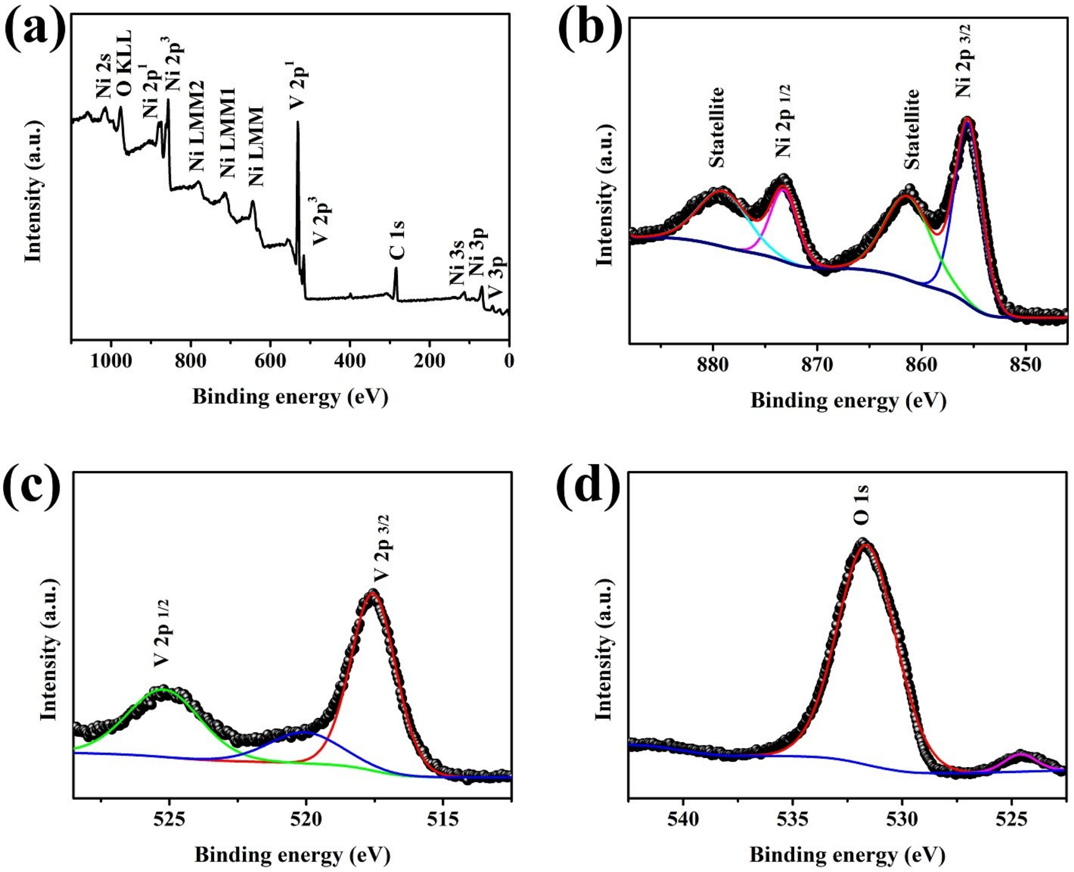

Figure S16 a)The XPS survey spectrum of $Ni_3(VO_4)_2$ after PEC test. High-resolution XPS spectrum of Ni 2p region b), V 2p region c), and O 1s region d).

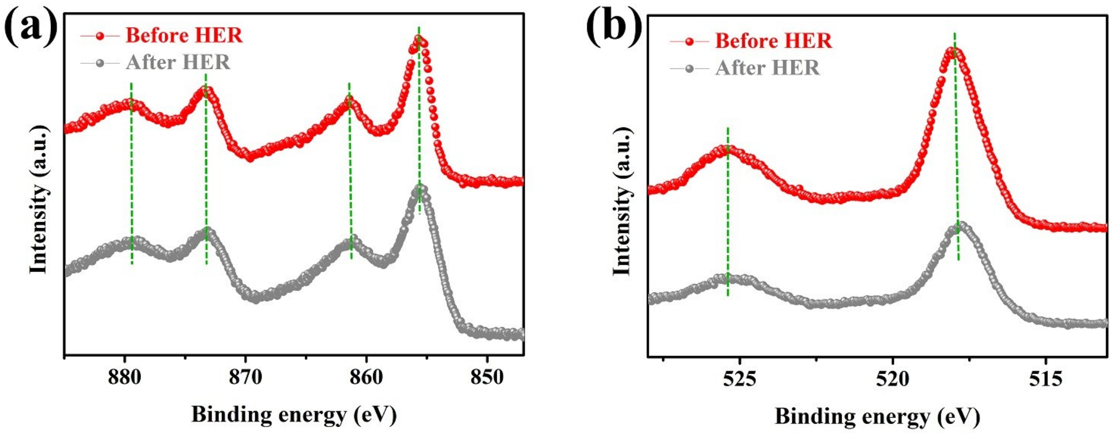

Figure S17 High-resolution XPS spectrum of Ni 2p region a), V 2p region b) of the sea-urchin shaped $Ni_3(VO_4)_2$ before and after the PEC stability test.

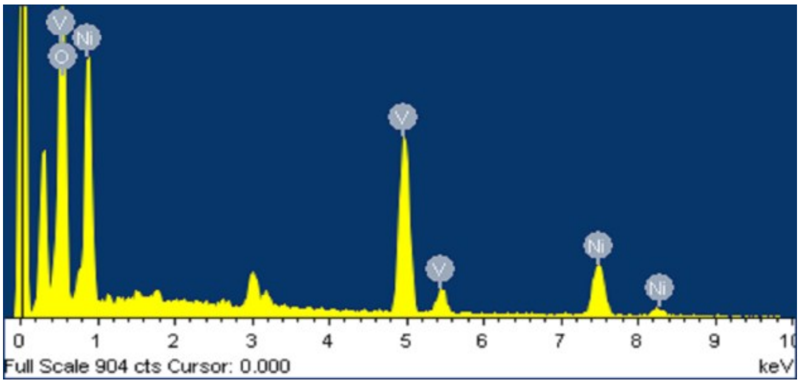

Figure S18 EDS spectrum of the sea-urchin shaped $Ni_3(VO_4)_2$ after the stability test.

Table S3. EDS elements analyze of the sea-urchin shaped $Ni_3(VO_4)_2$ after the stability test.

Element	Weight%	Atomic%
O K	38.66	68.62
V K	23.01	12.82
Ni K	38.33	18.55
Totals	100.00	

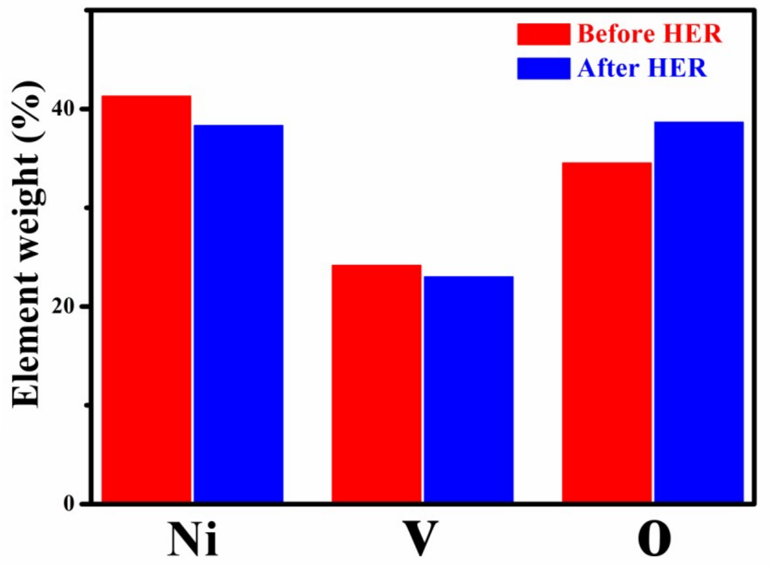

Figure S19 The comparison of the element weight ratio of the sea-urchin shaped $Ni_3(VO_4)_2$ before and after the stability test.

Figure S13 compares the SEM images of the sea-urchin shaped $Ni_3(VO_4)_2$ before and after stability test of photo-enhanced HER electrocatalysis. There are only tiny changes in the morphology of the structure, which may attribute to some strain relaxation of the thin nanoflakes on the spherical surface or the oxidation of $Ni_3(VO_4)_2$ during the HER process.[5] Fig. S14 exhibits XRD patterns of sea-urchin shaped $Ni_3(VO_4)_2$ before and after PEC stability test, tiny change can be found, which further confirms the chemical stability of catalyst. In addition to the SEM images, the structural stability is further supported by TEM (Fig. S15). Fig. S15 a-d illustrate that the main morphology was nicely maintained which is consistent with the SEM results. It's worth mentioning that the sea-urchin shaped sphere somewhat agglomerated and adhesion between the spheres appeared after PEC stability test. Although the nanoflakes on the surface slightly crimped, the lattice fringes with interplanar distances maintain in ~0.249 nm corresponding to the (122) planes of $Ni_3(VO_4)_2$ (Fig. S17 e-f).[6,7] As is shown in Figure S19, the major elements do not illustrate particular changes. Beside the oxidation of catalysts, the residual Nafion being used in HER electrocatalysis test may also produce the incremental oxygen.

S4 Photoelectrochemical properties of catalysts

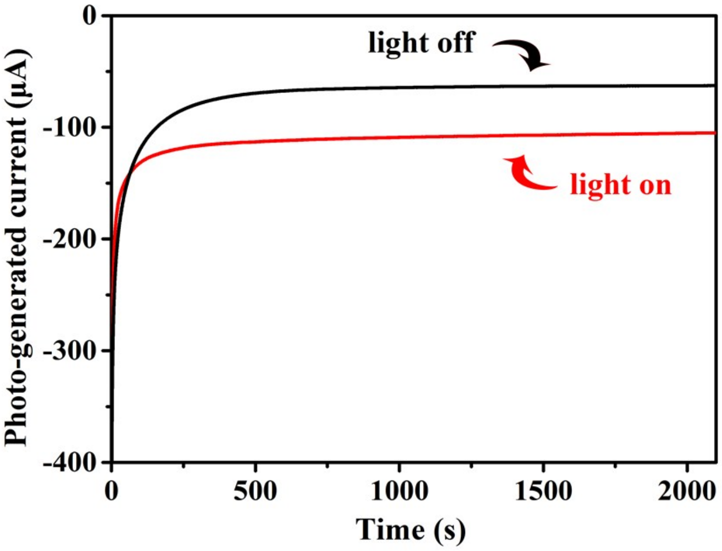

Figure S20 Time-dependent photocurrent responses curve under open circuit potential with/without visible light irradiation.

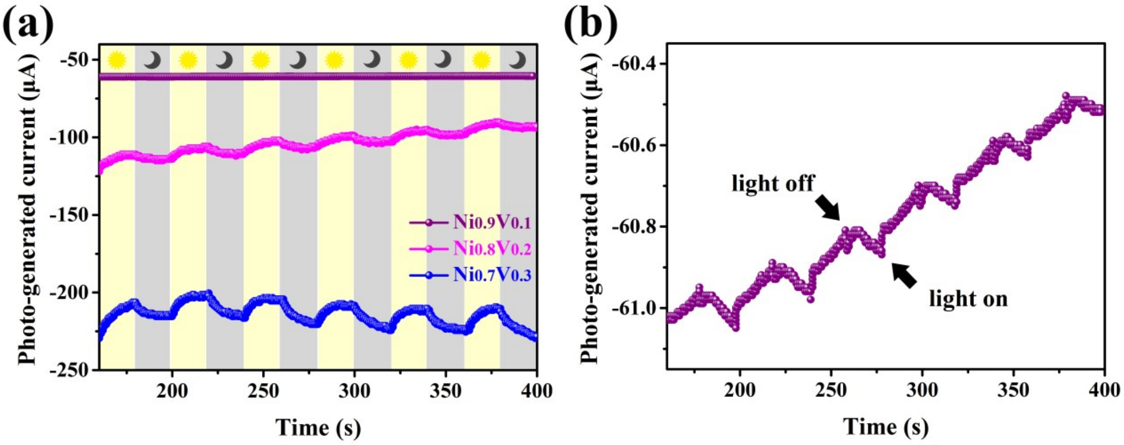

Figure S21 (a) Photocurrent responses of $Ni_{0.9}V_{0.1}$, $Ni_{0.8}V_{0.2}$ and $Ni_{0.7}V_{0.3}$ in 0.5 M Na_2SO_4 solution under visible light irradiation. (b) Photo-generated current-time curve of $Ni_{0.9}V_{0.1}$ within a small range scale.

As a proof-of-concept application, the FTO photoanode of PEC cell was used to examine the photocurrent characteristics. Figure S20 illustrate the photo-generated current-time curves, where the black and red lines represent the current density in the dark and under illumination, respectively. The enhanced photocurrent could be seen at any external potentials, indicating the effective photoresponse ability. For a distinct comparison, the photo-generated current-time curves of $Ni_{0.9}V_{0.1}$ within a small range scale was shown in Fig. S21b. Almost no photocurrent response of is detected on bare FTO substrate, excluding the contribution from FTO.

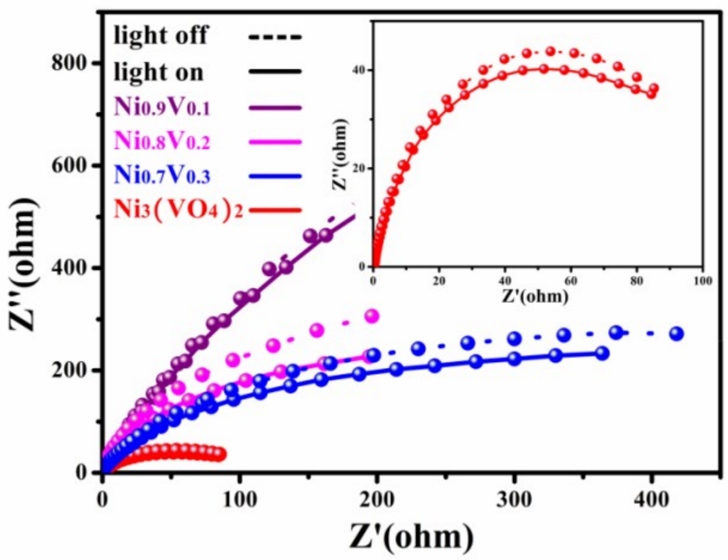

Figure S22 Nyquist plots of the sea-urchin shaped $Ni_3(VO_4)_2$ and Ni_xV_{1-x} materials ($Ni_{0.9}V_{0.1}$, $Ni_{0.8}V_{0.2}$ and $Ni_{0.7}V_{0.3}$) before and after visible light irradiation.

As is shown in Figure S22, all the catalysts display a lower charge transfer resistance (Rct) after light irradiation than before, and the $Ni_3(VO_4)_2$ catalyst reveal lower faradaic impedance than other catalysts. The small Rct value observed for the $Ni_3(VO_4)_2$ after light irradiation implies good electron transfer ability,[8] suggesting the composite is indeed a highly efficient photoresponse electrocatalyst in the hydrogen evolution reaction.

Reference

1 P. Yu, X. Zhang, D. L. Wang, L. Wang, Y. W. Ma, *Cryst. Growth Des.*, 2009, **9**, 528-533.

2 X. C. Song, Y. Zhao, Y. F. Zheng, *Cryst. Growth Des.*, 2007, **7**, 159-162.

3 S. Y. Kim, C. B. Park, M. K. Lee, I. Song, J. G. Kim, M. H. Lee, J. H. Jung, Y. S. Kim, H. S. Lim, H. C. Choi, *Adv. Funct. Mater.*, 2017, 1700925-1700932.

4 D. P. Dubal, G. S. Gund, C. D. Lokhande, R. Holze, *ACS Appl. Mater.*

Interfaces, 2013, **5**, 2446-2454.

5 Y. W. Tan, P. Liu, L. Y. Chen, W. T. Cong, Y. Ito, J. H. Han, X. W. Guo, Z.Tang, T. Fujita, A. Hirata, M. W. Chen, *Adv. Mater.*, 2014, **26**, 8023-8028.

6 E. Baudrin, M. Touboul, G. Nowogrocki, *J. Solid State Chem.*, 2000, **152**, 511-516.

7 W. B. Zhang, L. B. Kong, X. J. Ma, Y. C. Luo, L. Kang, *New J. Chem.*, 2014, **38**, 3236-3241.

8 S. A. Ansari, M. M. Khan, M. O. Ansari, J. Lee, M. H. Cho, *New J. Chem*., 2014, **38**, 2462-2469.